



Impact of rainstorm patterns on the urban flood process superimposed by flash floods and urban waterlogging based on a coupled hydrologic–hydraulic model: a case study in a coastal mountainous river basin within southeastern China

Weiwei Jiang¹ · Jingshan Yu¹

Received: 15 September 2021 / Accepted: 16 December 2021 / Published online: 27 January 2022
© The Author(s), under exclusive licence to Springer Nature B.V. 2021

Abstract

Flash floods (FF) and urban waterlogging (UW) hazards pose a serious threat to citizens and property, becoming a global challenge. However, the rainstorm patterns that influence the urban flood process associated with both FF and UW are still not well understood. This paper utilized and verified a coupled hydrologic–hydraulic model to determine the FF hydrographs, inundation indicators, and statistical relationship of surface inundation under different return periods as well as rainstorm patterns in a mountainous city experiencing both FF and UW. The results show that the effects of the rain peak coefficients on FF hydrographs and urban surface inundation indicators are relatively similar. FF volumes and urban inundation severity increase with an increasing rain peak coefficient, while the lag time of FF hydrograph and inundation depth becomes shorter. The effect of rainstorm patterns on surface inundation has been considerably amplified by FF, especially for high return periods and inundation areas with a high-water depth. When FF and UW superimpose on urban inundation, the impact of the rainstorm patterns on the spatial distribution of the inundation lag time shows a distinctive response due to the different district topographies on the FF propagation pathway. Furthermore, FF dominated the total inundation volume and thus significantly increases the surface inundation spatial connection of different locations. The exponential relationships for maximum inundation depth of many flooding vulnerable points were found. The key findings of this study provide a readymade technical tool and thus aid decision-makers in managing urban flood problems on a basin scale.

Keywords Rainstorm patterns · Flash flood hazards · Urban waterlogging · Urban flood processes · Hydrologic–hydraulic modeling · Coastal mountainous basin

✉ Jingshan Yu
yujingshanbnu@163.com

¹ Key Laboratory of Urban Hydrological Cycle and Sponge City Technology, College of Water Sciences, Beijing Normal University, Beijing 100875, China

1 Introduction

Flooding is one of the most common and destructive natural disasters globally, resulting in significant damage, threatening human life, and severe property loss. Flooding disasters are gaining widespread attention since they are characterized by strong outbreaks, significant peak values, and wide damage areas (Bajabaa et al. 2014; Salvadore et al. 2015; Yin et al. 2016). In recent decades, the frequency of urban flooding has become more frequent due to various factors and their combinatorial effects. These factors include continued watershed development with increasing impervious surfaces (Ebrahimiyan et al. 2018), local rain island effects, an increasing complex underlying surface caused by urbanization (Bayazit et al. 2021; Yang et al. 2011; Zhao et al. 2021), population growth which brings significant pressure on communities to develop in flood-prone areas (Gallegos et al. 2009; Sahoo and Sreeja 2016), climate change that enhances the probability of highly intense and extreme rainstorms (Zhou et al. 2019), and degraded artificial infrastructure that cannot keep up with urban drainage demands (Cheng et al. 2020). China is now experiencing rapid urbanization and has suffered from numerous severe flood disasters in recent years (Xing et al. 2021; Zhang et al. 2020). According to a recent report by the Ministry of Emergency Management of China in 2020, there were 38.26 million people affected by floods and waterlogging causing an economic loss of 109.7 billion Chinese Yuan. Therefore, more in-depth research is needed to solve urban flooding, which is still a challenging task for researchers and policymakers in the context of climate change and rapid urbanization.

Previous studies that explored flooding disasters are focused on urban waterlogging (UW) and flash floods (FF) since the two events have different characteristics, magnitudes, and scales (Ma et al. 2018). FF is recognized as a rapid flood caused by heavy rain within a short time period (generally less than six hours), rapid evolution, and occurring in large-scale basins or mountainous areas (Hu and Song 2018; Smith et al. 2013; Haque et al. 2020). UW is caused by local excessive and continuous rainfall, which exceeds the drainage systems capacity and appears in the plain area on an urban scale (Chen et al. 2018; Yin et al. 2016; Zhang et al. 2020). Studies associated with FF deal with rainfall–runoff relationships in order to simulate hydrograph discharge, while UW is primarily focused on spatial distributions of inundations and its response to environmental variables, including rainfall, underlying surfaces, and drainage systems within urban surface inundations (Bruwier et al. 2018; Leandro et al. 2016; Müller and Haberlandt 2018). For instance, FFs are sensitive to the spatial and temporal variations of rainstorms within small basins. A conclusion was drawn that the largest peak flows were strongly associated with the storm core position; however, they have little relation to rainstorm movement (Veldhuis et al. 2018). Peak discharge of an FF hydrograph has an excellent correlation with temporal rainfall resolution of less than 30 min (Yang et al. 2016). Conversely, UW inundation events are significantly related to the working state of the underground drainage system (Chen et al. 2018; Cheng et al. 2020). Total impervious areas are a controlling factor affecting total runoff compared to the directly connected impervious areas within an urban community (Yao et al. 2016). It can be seen that most of the previous studies were carried out separately on FF or UW response to environmental variables with few researchers combining the two events (Ma et al. 2018). Hence, further studies are needed to unravel the complex interactions of the inundation responses and flood management; thus, addressing the challenging problems for those cities affected by both FF and UW.

Many studies revealed that rainfall spatial–temporal distribution, rainstorm intensity, and impervious ratio are the dominant factors for urban inundation magnitude (Veldhuis

et al. 2018; Smith et al. 2013; Zhang et al. 2019). The surface underlying characteristics including topography, microtopography, roughness, buildings, and drainage systems are key factors in determining the inundation frequency and location where the flooding occurs (Cao et al. 2021; Gallegos et al. 2009; Palla et al. 2016). Extreme rainfall events are a key reason for urban flooding, while the effects of rain characteristics seem to be more important (Mei et al. 2020; Zhang et al. 2019). The investigation of FF hydrographs, maximum inundation depth, inundation extent, lag time, and inundation statistical relationships is the primary concerns and indicators for studying the response of FF and UW regarding rain events (Sahoo and Sreeja 2016). It has been found that the temporal distribution of rainfall is vital for designing drainage systems since larger rain peak coefficients cause greater fully filled pipe ratios (Chen et al. 2018) as well as a severe decrease in the performance of drainage systems (Cheng et al. 2020). The shorter the rainfall duration for the same total rainfall amount, the more severe the surface inundation is (Mei et al. 2020). However, studies associated with the response of rain patterns on integrating UW and FF are relatively scarce. Furthermore, a vast amount of the literature is devoted to exploring the mutual relationships between rainfall, runoff, surface inundations, and drainage system performance (Saksena and Merwade 2015; Yao et al. 2016; Zhang et al. 2019). Although under various return periods and rain patterns, the inundation areas with a high-water depth are strongly positively correlated with the overflowed manhole volumes (Cheng et al. 2020). The relationship between rainfall intensity and maximum water depth of the entire inundation area shows an exponential trend even when changing land use (Sahoo and Sreeja 2016). The abovementioned relationships provide a better understanding and are of significant importance for the management and prevention of floods. However, there is no formal rule or relationship to identify the maximum inundation depth between various flood-prone locations under different rainstorm characteristics.

Coastal mountainous areas in southeastern China are prone to typhoons and short-term heavy rainstorms, characterized by rapid FF with a short lag time (Mei et al. 2020; Shang et al. 2019). Many small-scale cities and towns are distributed on the alluvial plain in the downstream reaches of those mountainous basins. These cities often encounter both FF and UW having a high flood risk since they have low-lying land, high economic growth, high population density, and a low drainage capacity of the drainage systems (Ma et al. 2018). Numerical simulation provides technological support for flood hazard mapping playing an important role in flood forecasting and early warnings (Dimitriadis et al. 2016). The FF hydrographs are generally calculated by hydrologic simulation for a given set of rainfall data within a basin. The UW and inundation depth estimations are based on more complex bidimensional hydraulic modeling depending on the detailed topographic map of the floodplains and urban areas (Xing et al. 2021; Yin et al. 2016). As a result, a coupled hydrologic and hydraulic approach was proposed to deal with the rainfall–runoff–inundation processes on a basin scale (Montanari et al. 2009; Grimaldi et al. 2013). The approach assumed that each hydrological response unit of the entire basin does not interfere with each other and thus has the advantage of saving simulation time and reducing input data requirements (Chi and Mantilla 2015; Jiang et al. 2021).

The Meixi basin is a coastal mountainous basin including mountainous areas in the upstream and a small town within the downstream reach of the basin and is affected by both FF and UW. The rainfall–runoff–inundation processes in the Meixi basin associated with the FF and UW were simulated via coupled hydrologic–hydraulic modeling. The objective of this paper is to (1) illustrate the response of the FF hydrograph and UW inundation indicators (total inundation volume, inundation extent, lag time, and inundation depth) to different rainstorm characteristics (different return periods and rain peak coefficients);

(2) unravel the complex interactions of the urban surface inundation superimposed with FF and UW; (3) determine the possible relationship of the maximum inundation depths of various flood-prone locations under different rainstorm characteristics. The knowledge gained from this study can provide valuable information for decision-making related to the management of urban flood issues, as well as other similar mountainous cities that also face the problems of FF and UW.

2 Study area, materials and methodologies

2.1 Study area

The Meixi basin, belonging to the city of Quanzhou in the Fujian Province, is located in the southeastern coastal area of China with an area of 101 km² (Fig. 1a, b and c). It is a small-scale mountainous basin, having a high elevation terrain in the north and southeast regions. The primary land-use types in the Meixi basin are covered in forest and cultivated land. The downstream reach of the basin is an alluvial plain. In this plain, an urbanized residential town exists having high impervious proportions (Fig. 1d). According to the significant spatial differences of the terrain, land use, and flood risk to the social economy, the Meixi basin can be characterized by mountainous and urbanized areas (Fig. 1c). Among them, the mountainous area (TMA) can be divided into five sub-basins (S1–S5) based on the terrain defined by the Hydrology tool of Spatial Analysis Tools within the ArcGIS 10.2 software (Bajabaa et al. 2014). The Meixi and Siduxi Rivers originate from the S2 and

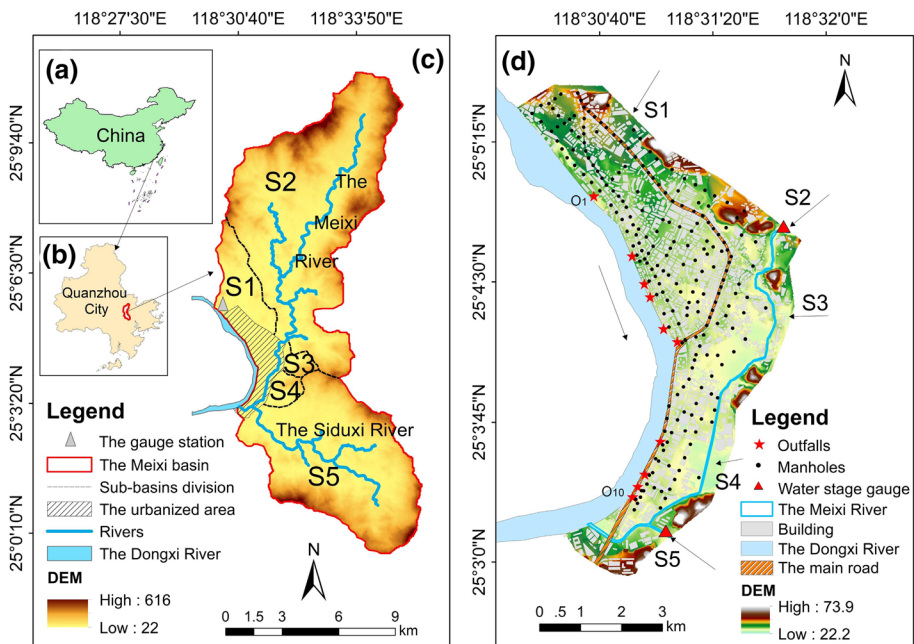


Fig. 1 Location of the Meixi basin (a and b), sub-basins division in the mountainous area (c) and the urbanized area (d)

S5 sub-basins, respectively. The rivers empty into the Dongxi River, which is the outlet boundary of the Meixi basin. S1, S3, and S4 sub-basins are relatively small and have no natural river channel. However, FF can take place and directly propagate into the urbanized area (TUA) when rainstorm events occur (Fig. 1d). TUA is a town with an area of 5.4 km² low elevation, dense buildings, and a large impervious proportion (Table 1). Moreover, the underground drainage systems capacity in the TUA is insufficient and lacks proper management. The sub-basins S1–S5 (1.4–55.6 km²) are characterized by steep slopes, fast flow, and rapid convergence, leading to FF within a short lag time. Furthermore, the TUA will be jointly vulnerable to UW by local rainstorms and external FFs from the surrounding five sub-basins in the TMA.

The study area is characterized by a subtropical marine monsoon climate and is vulnerable to typhoons 2–3 times per year (Ma et al. 2018). The area has an annual precipitation of 1000–1800 mm. Typhoons, thunderstorms, and short-term heavy rain events are primarily concentrated from May to September. For example, typhoon Molanti brought a rainfall with a 16-h duration and a total rainfall amount of 259 mm (rainstorm 20,160,915), causing a catastrophic flood in 2016, resulting in 13 dead or missing as well as a substantial economic loss of 6 billion within the Meixi basin. Therefore, it is beneficial to research the response between different rainstorm patterns and the two superimposed inundation effects caused by FF and UW. Figure 2 shows the framework of the FF and the urban surface inundation responses to the different rainstorm characteristics within this study. The framework comprises four steps: Step 1 and Step 2 describe the collection of essential simulation data and the details of the coupled model (Sects. 2.2 and 2.3). Based on different designed rainstorm events in Step 3, the effect of rainstorm patterns on the surface inundation indicators is analyzed and discussed in Step 4 (Sects. 3.2 and 3.3).

2.2 Data collection and preprocessing

2.2.1 Geographic data

The basic geographic data used in TMA include a digital elevation model (DEM), land use, and soil type, all of which have a 30 m resolution and are obtained from open access resources (<http://www.gscloud.cn/> and <http://vdb3.soil.csdb.cn/>). A water-stage automatic recorder (HOBO U20, one data per five minutes) was installed in the channel of the two rivers at the boundary between S2 and TUA, and S5 and TUA from Mar 2018 to Sep 2019 (Fig. 1d). The collected water-stage data can be transformed into discharge data through corresponding the cross section geometry (Brinkerhoff et al. 2019). Furthermore, the urban hydrodynamic simulation needs high-resolution data to delicately delineate the complex underlying surface and microtopographies (Kim et al. 2021; Salvatore et al. 2015). In the TUA, the high-resolution DEM data (1 m) and the high-definition images (0.2 m) were collected by an unmanned aerial vehicle (UAV) equipped with oblique photography technology conducted in November 2018. Land-use types and building profiles in the TUA were extracted from high-definition images using ArcGIS 10.2 software.

2.2.2 Drainage system data

The drainage system data, provided by the local Drainage Management Bureau, contained geographic and geometric information on the pipes and manholes (Fig. 1d). The diameters of the pipes ranged from 300 to 1200 mm, and the slope of the pipes ranged from 0.1% to

Table 1 Summary characteristics of the mountainous sub-basins and the urbanized area within the Meixi basin

	The mountainous area (TMA)					The urbanized area (TUA)	
	S1	S2	S3	S4	S5		
Sub-basin ID	S1	S2	S3	S4	S5	–	
Area (km ²)	6.5	55.1	1.4	1.9	38.4	5.4	
Slope (m/m)	0.028	0.033	0.084	0.073	0.036	0.012	
Basin length (km)	5.8	17.5	1.4	1.6	12.5	5.3	
Percentage of cropland (%) ^a	70.0	47.6	57.7	58.4	47.8	31.2	
Percentage of forest and grassland (%) ^a	24.7	46.1	42.2	41.55	49.7	10.7	
Percentage of impervious area (%) ^a	4.3	5.6	0.1	0.1	2.3	56.8	
Description	Characterized by low developed and steep slopes, resulting in rapid convergence into a flash flood, thus flowing into the urbanized area					Has high flood risk because of low elevation, dense buildings, and a large population, face the combined problems of external flash floods and local waterlogging	

^aRatio of the land-use type area to corresponding sub-basin area

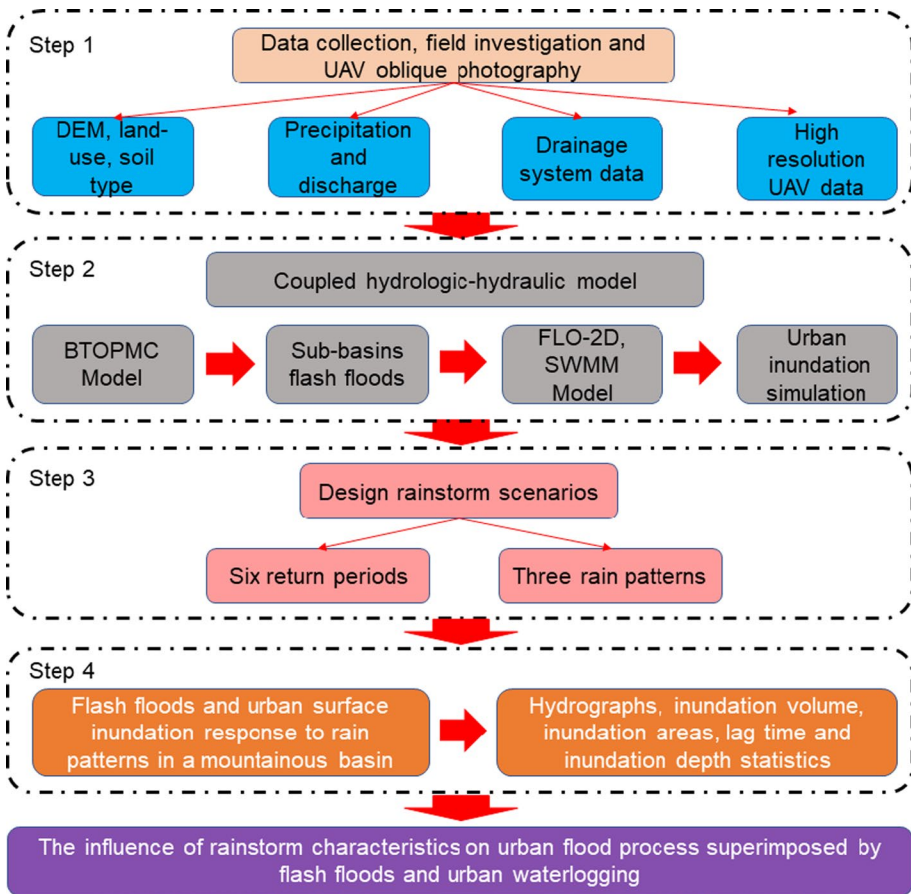


Fig. 2 Framework of the flash flood and urban surface inundation response to different rainstorm characteristics

2.5%. In total 229 manholes and 10 outfalls (O1~O10) along the Dongxi riverbank were included in the drainage system, which has a total pipe length of 27.5 km and a drainage network density of 5.22 km/km². It is necessary to mention that the drainage pipe design standard in the TUA is only for 1 year of rainfall.

2.2.3 Rainstorm data

One recorded historical disastrous rainstorm 20,160,915 was used for validation purposes. The rainstorm data have an interval of 1 h and were obtained from the Honglai Gauging Station (Fig. 1c). The observed water stage at the station and the difference between this water-stage data along the Dongxi River (Honglai Section) were also collected from the same station and the local Drainage Management Bureau. Water stage at specific points (O1~O10) along the Dongxi River can be estimated and was set as the downstream boundary condition for both the drainage system outfalls and the Meixi River. Rainstorm 20,160,915 has a bimodal distribution with a maximum intensity of 59 mm/h, long

duration, and a significant total rainfall amount (Fig. 3); thus, rainstorm 20,160,915 caused severe inundation and damage. Additionally, historical inundation traces were recorded during the rainstorm 20,160,915 within the TUA. The maximum inundation depth at ten different locations was estimated from flood traces of buildings through field investigations and from news-reported pictures (Fig. 4).

To investigate how rainstorm patterns impact the inundation processes associated with UW and FF, three patterns of rainstorms with different rain peak coefficients ($r=0.2$, $r=0.5$, and $r=0.8$) and six return periods (from 1 to 100 years) were generated as model inputs for scenario simulation (Fig. 5). The previous study demonstrated that rainstorms in Xiamen (adjacent to Quanzhou city) are primarily single peaks (Shang et al. 2019). Short-term heavy rainstorms should be given more attention concerning FFs within the coastal mountainous basins in the Fujian province (Mei et al. 2020). Although rainstorm 20,160,915 was bimodal and had durations as long as 16-h, a single-peak rainstorm with a 3-h duration was designed for this study. According to the Bureau of Municipal and Rural Construction of Quanzhou City, the rainfall intensity in the Meixi basin is summarized using Eq. (1). The Chicago approach (Keifer and Chu 1957) was used to redistribute the rainfall amounts before and after the peaks. The details of the designed rainstorm rainfall events are shown in Fig. 5.

$$q = \frac{2280.128 \times (1 + 0.724 \lg P)}{(t + 13.364)^{0.699}} \quad (1)$$

where q is the rainfall intensity (mm/min); P is the return period (yr); and t is the rainstorm duration (min).

2.3 Coupled hydrologic–hydraulic model

2.3.1 BTOPMC model

BTOPMC is a distributed watershed hydrological model that can reflect the non-uniform characteristics of hydrometeorology and basin underlying surfaces. The control equations and a more detailed introduction of this model can be seen in Takeuchi et al. (2010). The model is suitable for a mountainous watershed with large terrain differences. Simulation results of the

Fig. 3 Hydrographs of the rainfall and simulated flash floods of each mountainous sub-basin during rainstorm 20,160,915

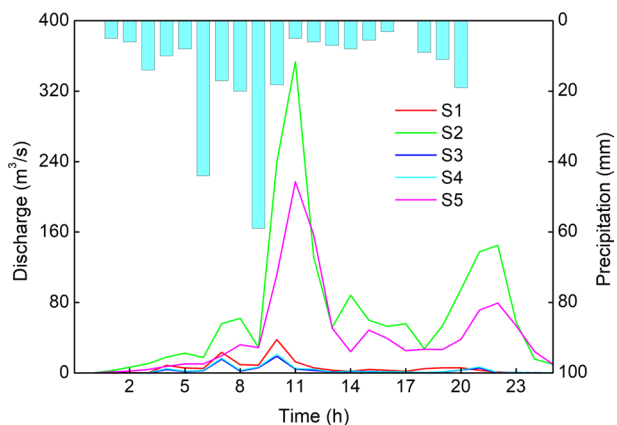


Fig. 4 The map of the simulated maximum inundation depth within the urbanized area during rainstorm 20,160,915

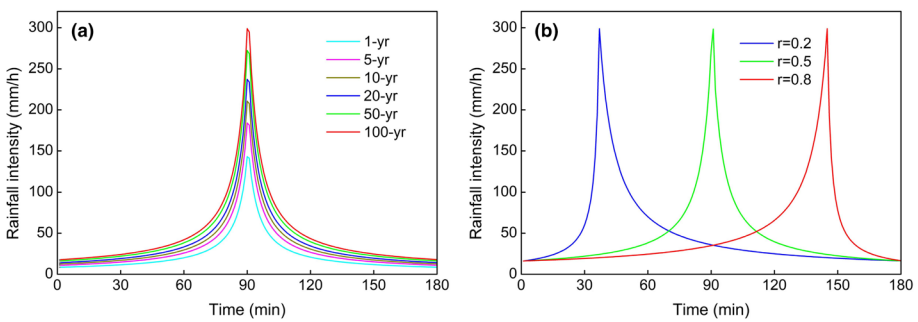
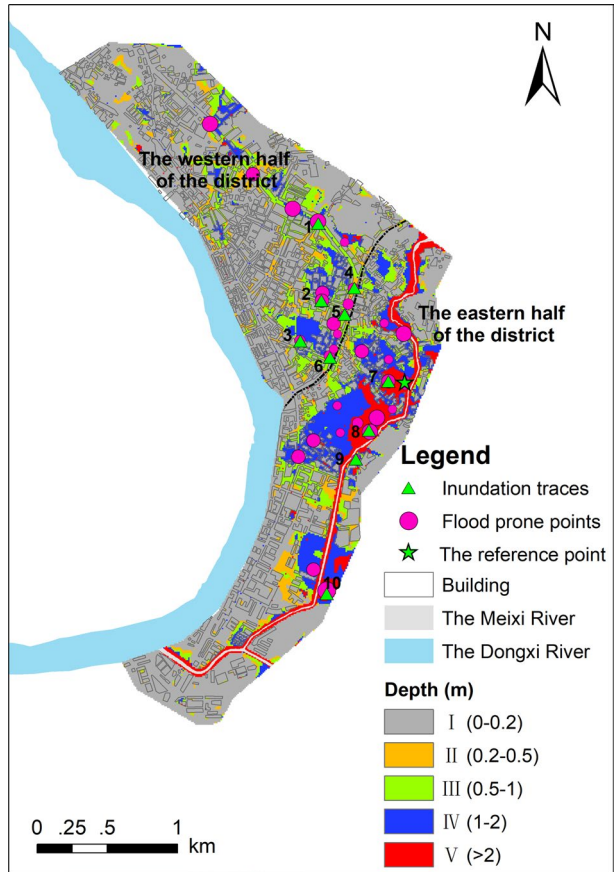


Fig. 5 Designed rainstorm events: **a** different return periods and **b** different rain peak coefficients

model were proven to be sufficient for the Jingjiang basin belonging to Quanzhou city (Sun et al. 2014). Therefore, the BTOPMC hydrological model was selected and utilized to calculate the rainfall–runoff processes of each sub-basin (S1–S5) in the TMA. In this study, the meshes of the BTOPMC model were set to 30 m. The resolution of the output FF discharge

data depends on the resolution of the input rainfall data, which was 5 min for the following rainstorm design scenarios.

2.3.2 FLO-2D model

FLO-2D is a raster-based commercial hydrodynamic software that allows for the flexible geometry of the channel and the floodplain terrain (FLO-2D Software Inc, 2012). It can describe the flow wave propagation of the channel and floodplain in more detail and thus is widely used for mountainous storm surge simulations and river channel overbank inundations (Dimitriadis et al. 2016; Grimaidi et al. 2013; Peng and Lu 2013). In this study, we used FLO-2D for surface flood inundation modeling in the TUA. High-resolution DEM data (1 m) were imported to the model, and a total of 51,265 meshes were generated. Studies associated with urban flooding commonly regard buildings as impermeable walls or blocks (Shen and Tan 2020). In this study, meshes inside buildings are regarded as blocks and non-flooding zones within the FLO-2D model. The infiltration calculation method used in the FLO-2D model is the Green–Ampt method. The model solves the average velocity u in the x -axis direction, the average velocity v in the y -axis direction, and the flow depth h (O'Brien et al. 1993; Peng and Lu 2013; Zhang et al. 2015). The governing equations are given as follows:

$$\frac{\partial h}{\partial t} + \frac{\partial(uh)}{\partial t} + \frac{\partial(vh)}{\partial t} = i \quad (2)$$

$$S_{fx} = S_{bx} - \frac{\partial h}{\partial x} - \frac{u}{g} \frac{\partial u}{\partial x} - \frac{v}{g} \frac{\partial u}{\partial y} - \frac{1}{g} \frac{\partial u}{\partial t} \quad (3)$$

$$S_{fy} = S_{by} - \frac{\partial h}{\partial y} - \frac{v}{g} \frac{\partial v}{\partial y} - \frac{u}{g} \frac{\partial v}{\partial x} - \frac{1}{g} \frac{\partial v}{\partial t} \quad (4)$$

where h is flow depth (m), u is average flow velocity in the x -axis direction (m/s), v is average flow velocity in the y -axis direction, and i is rainfall intensity (mm/h). S_{fx} , S_{fy} are the friction slopes of the x - and y -axis directions; S_{bx} , S_{by} are the bed slopes of the x - and y -axis directions; and g is the acceleration of gravity (m/s^2).

2.3.3 SWMM model

The FLO-2D model is internally coupled with the modular EPA SWMM (FLO-2D Software Inc, 2012). SWMM is a dynamic hydrology–hydraulic water quality model used worldwide (Chen et al. 2018; Zhang et al. 2019). Sewer flow in the underground drainage system and the node overflow to the surface were simulated using SWMM modular in the FLO-2D model. The SWMM modular solves the Saint–Venant equations using the implicit finite difference method. The governing equations are given as follows:

$$\frac{\partial A}{\partial t} + \frac{\partial Q}{\partial x} = 0 \quad (5)$$

$$\frac{1}{gA} \frac{\partial Q}{\partial t} + \frac{Q}{gA} \frac{\partial}{\partial x} \left(\frac{Q}{A} \right) + \frac{\partial h}{\partial x} = S_0 - S_f \quad (6)$$

where Q is the flow rate (m^3/s), A is the flow cross-sectional area (m^2), x is the longitudinal distance (m), H is the hydraulic head of water in the conduit (m), g is the acceleration of gravity (m/s^2), S_f is the friction slope, and S_0 is the slope of the pipe.

2.3.4 Models coupling strategy

The integrated flooding process in the TUA involves the waterlogging caused by local rainstorms and the FF originating from the mountainous sub-basins. Moreover, we utilized and followed the coupled hydrologic–hydraulic and event-based approach (Chi and Mantilla 2015; Grimaldi et al. 2013; Jiang et al. 2021), i.e., the output discharge hydrograph from the TMA simulated by the BTOPMC model provides the input data for the FLO-2D model at the boundaries between the five sub-basins and the TUA (Fig. 1d). Furthermore, underground sewer flow, overflow to the surface and return flow from the surface through the manholes was also considered bidirectionally in the TUA since the SWMM modular was internally coupled within the FLO-2D model. Floodplain runoff discharge from the surface enters the pipeline system at the inlets. The inlet discharge is imposed as the surface water boundary conditions and is passed to the storm drain layer for routing by the SWMM module. Weir and orifice equations are used to calculate an inflow discharge under inlet control (FLO-2D Software Inc, 2012). If the drainage system is surcharged, the excess water will overflow from the manholes to the surface and may exacerbate urban inundation. As a result, the coupled model can simulate the rainfall–runoff–inundation processes and the interactions of FF and UW precisely and realistically for the entire Meixi basin.

3 Results

3.1 The coupled model verification

In the TMA, an earlier study pointed out that the key parameters of the BTOPMC model are saturated transmissivity, maximum root zone storage, decay factor of transmissivity, and channel roughness (Takeuchi et al. 2010). Here, the parameters in sub-basin S2 and S5 were calibrated and verified according to the discharge data obtained from the channels water-stage recorder. It can be seen that the Nash–Sutcliffe coefficient (NSE) is within the range of 0.63–0.78 within the calibration and validation periods for S2 and S5 sub-basins (Fig. 6). The calculated NSEs are close to that in an early study (Sun et al. 2014), indicating the simulation results of the BTOPMC model can be used for further scenarios. The other three sub-basins S1, S3, and S4 did not have natural channels; however, S1 and S3 are adjacent to S2 in the north, and S4 is adjacent to S5. Parameter transfer was proven to be a valid method for the adjacent ungauged basins (Chouaib et al. 2018; Krebs et al. 2014); thus, we applied the method to the Meixi basin. The parameters after calibration and verification of the S1–S5 sub-basins are shown in Table 2.

The coupled hydrologic–hydraulic model was verified under the extreme events of rainstorm 20,160,915. FF hydrographs of sub-basins (S1–S5) from the TMA were calculated by the verified BTOPMC model (Fig. 3). The roughness of different land-use types, underground drainage pipes, and the Green–Ampt infiltration parameters in the TUA is shown in Table 3, all of which are based on the FLO-2D user manual and previous studies (Gayer et al. 2010; Mei et al. 2020). The simulated maximum water depth and the observed maximum water depth at ten locations are provided in Fig. 4 and Table 4. All the simulated

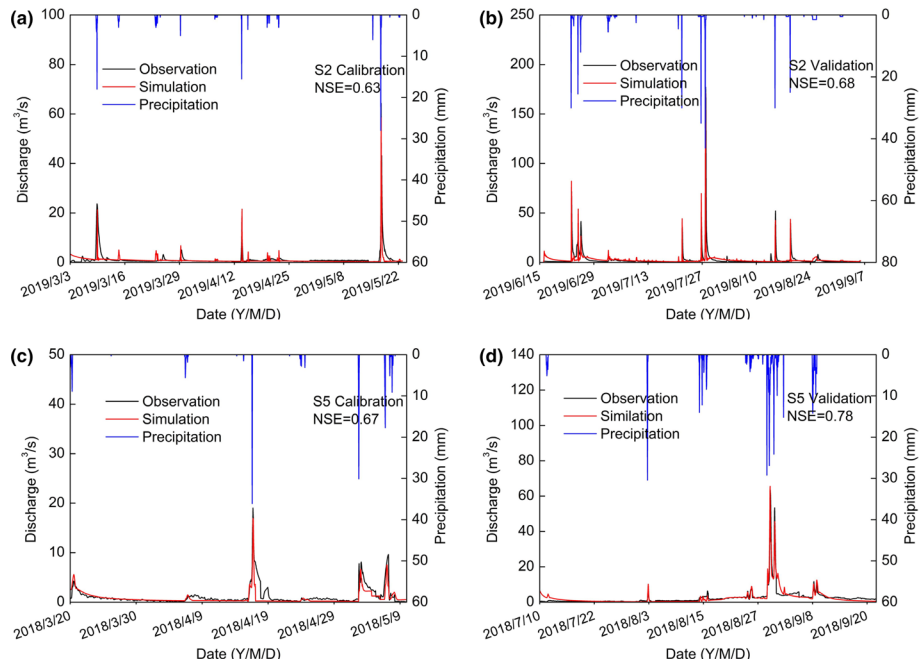


Fig. 6 Calibration and validation of the hydrologic model for sub-basins S2 and S5

Table 2 The parameters calibrated for the hydrologic model in the mountainous area

Parameter	Description		Sub-basins S1, S2 and S3	Sub-basins S4 and S5	Unit
T_0	Saturated transmissivity	Sand	15	10	$m^2 \cdot h^{-1}$
		Silt	10	15	
		Clay	8	10	
Srmax	Maximum root zone storage	Forest	0.02	0.01	m
		Grassland	0.01	0.01	
		Cropland	0.01	0.01	
m	Decay factor of transmissivity		0.022	0.020	–
α	Soil drying function parameter		4.3	3.5	–
n	Average manning coefficient		0.05	0.04	–
Δt	Temporal discretization of flow in a channel segment		1	1	–
Δl	Spatial discretization of a channel segment		1	1	–

results except Point 5 are close to what was observed, with a relative error of -12.4% to 11.7%. The inundation depth at the point 5 was affected by the flood volume from S1 and the overbanking volume from the Meixi River. The recorded inundation depth may be enhanced by the effect of bridge clogging at the channel near the reference point (Fig. 4). In the coupled model, the current modeling software did not provide the bridge clogging

Table 3 The parameters calibrated for the hydraulic model in the urbanized area

Parameter	Description and land use type	Value	Unit	
Manning coefficient	Impervious area	0.04	s/m ^{1/3}	
	Forest	0.4		
	Cropland	0.15		
	River channels	0.035		
	Drainage system pipe	0.013		
Green-Ampt infiltration parameters	Hydraulic Conductivity	Forest	4.5	mm/h
		Cropland	9.1	
	Soil Suction	Forest	88.9	mm
		Cropland	109.22	
	Porosity	Forest	35	%
		Cropland	35	
	Rainfall abstraction	Forest	5.3	mm
		Cropland	3.1	
	Soil depth	Forest	3	m
		Cropland	3	

Table 4 Comparison of simulated, calculated, and recorded maximum inundation depths within the urbanized area during rainstorm 20,160,915

Historical inundation traces (No.)	Recorded depth (m)	Simulated depth (m)	Relative error simulated results (%)	Calculated depth (m)	Relative error of calculated results (%)
1	1.05	0.92	−12.4	1.03	−1.0
2	1.60	1.55	−3.1	1.70	6.2
3	1.90	1.80	−5.3	1.68	−11.5
4	1.00	0.95	−5.0	0.86	−14.0
5	1.40	1.06	−24.2	1.10	−21.4
6	1.60	1.48	−7.5	1.76	10.0
7	2.80	3.02	7.9	2.93	4.6
8	1.80	2.01	11.7	1.84	2.2
9	1.70	1.88	10.6	1.65	−2.9
10	2.95	2.70	−8.5	2.99	1.4

simulation function; hence, the difference between the simulated depth and the recorded traces at the point 5 is relatively large. Compared with other studies, the range of the relative error is lower than that of Cheng et al. (2020), suggesting that the coupled model is relatively accurate in order to simulate the inundations within the Meixi basin.

3.2 FF results under different rainstorm patterns in TMA

The FF hydrographs from each sub-basin (S1-S5) were calculated under the 18 designed rainstorm events, including 3 rain peak coefficients and 6 return periods (Fig. 5). The

effects of different rainstorm patterns on hydrographs are similar for each sub-basin, and therefore, only S1 and S2 are shown as an example (Fig. 7). The statistical results of the three FF hydrographs indicators indicate that the total runoff volume and peak discharge increase with an increasing peak coefficient and the return period (Fig. 7a, b, d, and e). However, the hydrograph lag time (peak time difference between the rainstorm and FF peak discharge) decreases with an increasing peak coefficient (Fig. 7c and f). Furthermore, the values of the abovementioned hydrograph indicators differ from S1-S5 because of the varied scale for each sub-basin area (Table 1). In general, the hydrograph indicators of larger sub-basins have greater increments but lower increasing rates of response to different rainstorm patterns. This is in accordance with previous studies demonstrating that the rainstorm patterns have a greater influence on smaller sub-basins (Yang et al. 2016; Veldhuis et al. 2018).

3.3 Inundation results under different rainstorm patterns in TUA

The same 18 rainstorms events were also set as the input for the FLO-2D model in order to determine the surface inundation response to the rainstorm characteristics. Moreover, the input for the FLO-2D model includes local rainfall and the 5 hydrographs of FF (S1-S5) calculated by the corresponding rain data in the TUA (Fig. 3). Given the actual situation within the underlying surfaces of the TUA via mixing the water of both the local rainstorm and the external FF (scenario group, inundation was affected by joint UW and FF), it is difficult to recognize the individual effects of the UW, FF, and the integrated effects of UW and FF. Therefore, we set up another 18 scenarios which excluded the FF input from S1-S5 sub-basins and regarded it as a comparison (control group, inundation was only affected by UW). The spatio-temporal variations of the inundation results are compared and presented in the following subchapters.

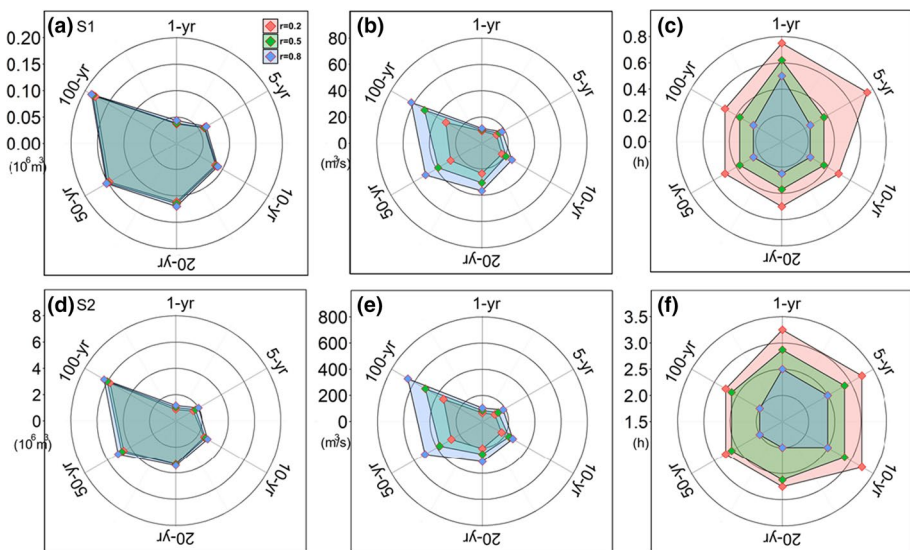


Fig. 7 Statistics of the flash flood hydrographs of sub-basins S1 and S2 under the designed rainstorm events. **a** and **d** total runoff volume, **b** and **e** peak discharge, **c** and **f** hydrograph lag time

3.3.1 Total inundation volumes

The total inundation volumes (TIV) in the TUA, that numerically reflecting the holistic severity, were obtained for the scenario group (TIV_S) and the control group (TIV_C) during the simulation period, respectively. The results show that both TIV_S and TIV_C increase as the rain peak coefficient and return period increase (Fig. 8). The ratio of TIV_S and TIV_C ranged from 1.02 to 9.39 and was significantly magnified when the return period was larger than 10 years due to abundant FFs starting to overbank along the Meixi River channel. This result also indicates that the local rainstorms dominate the surface inundation during low return periods, whereas FF dominates during return periods that are longer than 10 years in the TUA. The TIV_S and TIV_C responding to the rain peak coefficient have significant differences. TIV_S has a higher range of variation than TIV_C , suggesting the rainstorm patterns significantly impact inundation caused by FF rather than that of UW, especially in high return periods. For example, the peak coefficients increased from 0.2 to 0.8 ($P=50$ yr), the corresponding TIV_S and TIV_C increased from $2.35 \times 10^6 \text{ m}^3$ to $3.82 \times 10^6 \text{ m}^3$ and from $0.485 \times 10^6 \text{ m}^3$ to $0.497 \times 10^6 \text{ m}^3$. The increasing rates of TIV_S and TIV_C are 38.4% and 2.4%, respectively.

3.3.2 Spatial distribution of inundation areas and depth

Due to the low capacity of the underground drainage system, slight waterlogging can still occur in the TUA even during the low return periods at 1 and 5 years (Fig. 9). Therefore, this study primarily focuses on surface inundation and pays little attention to the performance of underground drainage systems. To understand the characteristics of the surface inundation spatiotemporally, the peak inundation areas were collected at different water depths based on previous studies (Chen et al. 2018; Mei et al. 2020). Five inundation grades were classified with I at 0–0.2 m, II at 0.2–0.5 m, III at 0.5–1 m, IV at 1–2 m, and V > 2 m. Moreover, external FFs that affected surface inundation primarily come from two directions with significant differences in the inflow hydrographs during rainstorm 20,160,915 (Fig. 3), including floods from the S1 sub-basin and the

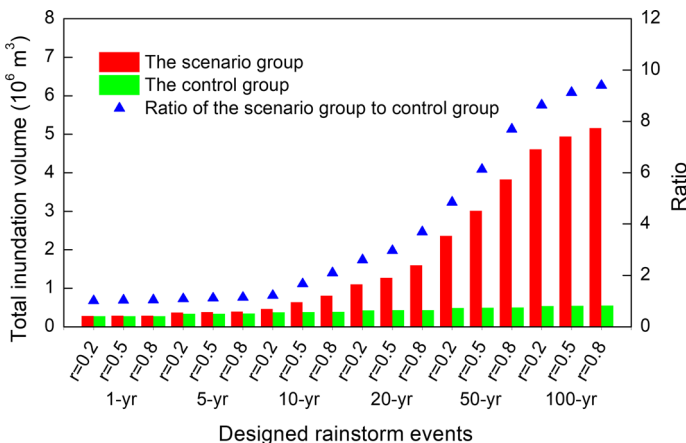


Fig. 8 The total inundation volume within the urbanized area under different designed rainstorm events for the scenario and control groups

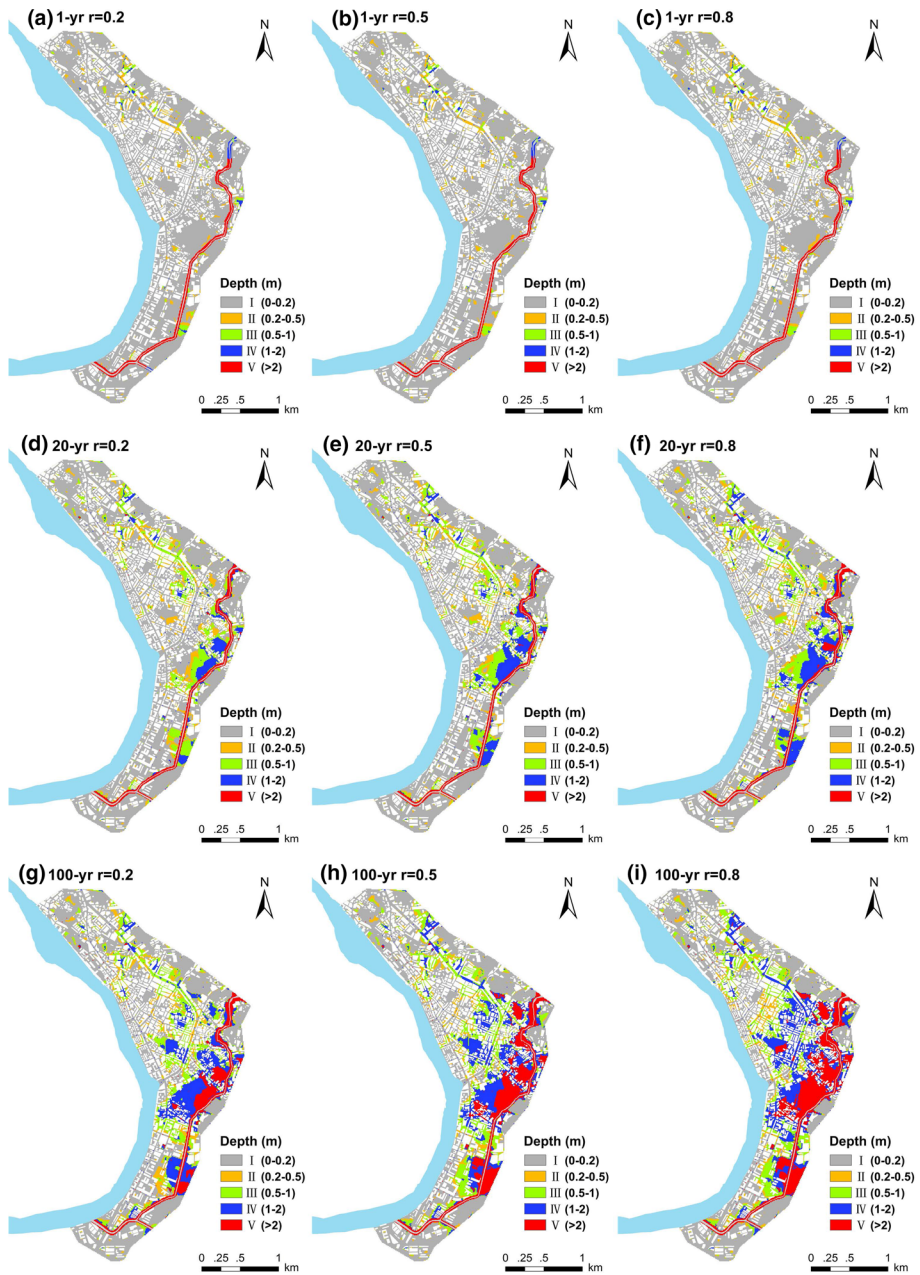


Fig. 9 Spatial distributions of inundation depths under different designed rainstorm events for the scenario group (only return period of 1, 20, and 100 years is presented)

overbank floods along the Meixi River from the S2 sub-basin, resulting in distinctive spatial distributions of inundation depth and flood concentration area. The western half of the district (accounting for 52% of the total area) and the eastern half of the district

(accounting for 48% of the total area) were divided in the TUA in order to identify the spatial inundation response to FFs and rain patterns (Fig. 4).

Figure 9 depicts the spatial distribution of the inundation areas with various grades under different return periods and rainstorm patterns for the scenario group. Results show no direct interaction between the FF from S1 and the overbank FF from S2, except for the 100 year return period. The statistical results for the control group indicate that the inundation areas for all inundation grades increased with the peak coefficients within the two districts and the entire urbanized area. When the FF was considered in the scenario groups, the inundation areas illustrated a similar response to the rainstorm patterns; thus, a higher peak coefficient leads to more severe inundation even during the same return period (Fig. 10a–c). Furthermore, the FF covered up the local waterlogging and thus plays a key role in enhancing inundation grades at both the magnitude and the increasing rates. The FF primarily increases the inundation areas at lower grades (II-III) in the western half of the district; however, in the eastern half of the district, a higher water depth (III-V) is observed (Fig. 10a, b). This is attributed to the differences of the floodplain elevation and the inflow FF volumes. The results from the control group showed that the rain peak coefficients have less influence on inundation with a high-water depth in grades IV and V (Fig. 10d–f). The inundation differences caused by the rain peak coefficient are negligible when the rain intensity is extremely high. However, it is not the case when the FF was superimposed. The increasing rate of inundation in grade V caused by the peak coefficients is 44% and 5% in the scenarios and control group (Fig. 10c and f), respectively. In terms of the total inundation area caused by the rain peak coefficient during a 100 year period, the increasing rate of the total inundation area is 23% and 3% in the scenarios and control group. Statistical results of the inundation areas are generally consistent with the TIV_S , indicating that the rain peak coefficients have a considerable impact on areas with high-water depths and return periods (Figs. 8 and 9).

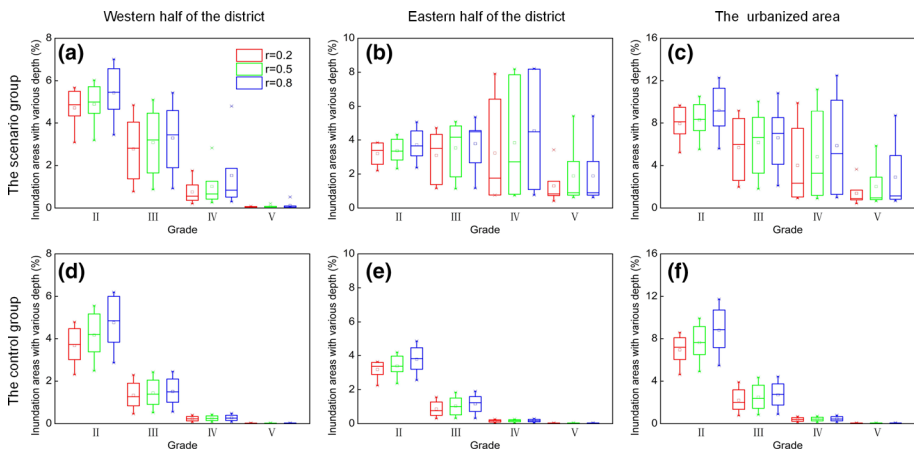


Fig. 10 The inundation area with various water depths and its percentage to the total inundation area under three rainstorm patterns for different districts and scenarios (each box plot consists of simulation results for six return periods)

3.3.3 Spatial distribution of inundation lag time

The spatial distribution of inundation results showed that the lag time varied considerably within the districts, return periods, and rainfall patterns (Fig. 11). In general, the inundation lag time (peak time difference between the rainstorm and the maximum inundation depth) displays a large difference of 2–4 h between the western half and the eastern halves of the districts, even within the same return periods, see 20 and 100 years in Fig. 11. The reason is that the surface inundation lag time varies with its original FF, as well as the difference in hydrograph lag time the S1 and S2 sub-basins being approximately 2 h (Fig. 7c and f). In addition, the control group results show that the inundation lag time decreases significantly with an increasing peak coefficient in both districts and the entire urbanized area (Fig. 12b, c, and d).

When FF and UW occur together in actual situations (scenario group), the spatial distribution of the inundation lag time did not fully display the expected variations. However, a similar trend exists in the west half of the district (Fig. 12a). There are, however, different trends of inundation lag time responses to rain peak coefficients that were found in the eastern half of the district and the entire urbanized area. Statistic results indicate that the inundation lag time of a mid-grade water depth (II and III) decreased after increasing peak coefficients (Fig. 12b, c). The variations can be related to the topography of the progress of the FF propagated pathways. In the western half of the district, FFs from the S1 sub-basin propagated to the main road following the slope and accumulating in the low-lying areas under gravities control (Fig. 1d and Fig. 11). Hence, the responding relationship between inundation lag time and peak coefficient is consistent (Fig. 12a and d). However, in the eastern half of the district, overbank FFs along the Meixi River propagate by overcoming terrain and gravity within the reverse slope (Fig. 1d and Fig. 11). When $r=0.5$ and 0.8 , the FF has a greater peak discharge and volume, resulting in a significantly larger inundation area upward from the river channel compared with that under $r=0.2$. Even in the same return period, some locations with high elevation were only affected by local rain under $r=0.2$; however, they were still covered by later FFs under $r=0.5$ and 0.8 (Fig. 9). Our results imply that the urban areas affected by external FFs from different directions, and the statistics of the inundation lag time for a whole area may hide some responsive differences of the underlying topographical characteristics and should be separated from the analysis (Fig. 11a, b, and c).

3.3.4 Inundation depth statistics

To investigate the statistical relationships within the surface maximum inundation depth (MID) between flood-prone positions under 18 designed rainstorm events, 31 flood-prone and low-lying points were selected. The points are distributed along the main road and near the Meixi River, all of which had high MID and flood risks during rainstorm 20,160,915 (Fig. 4). The determination coefficients (R^2) between the 18 pairs of MID of the 31 points were examined for the scenarios and control groups using the SPSS 20.0 software (Yao et al. 2016). The calculated R^2 of the 31 points is within the range of 0.32–0.77, and the average value is 0.56 for the control group. However, the range of the calculated R^2 in the scenario group remarkably increased to 0.81–0.97, with an average value of 0.90. These results demonstrate a weak relationship between the surface inundations spatially, whereas a very strong relationship between the surface inundations

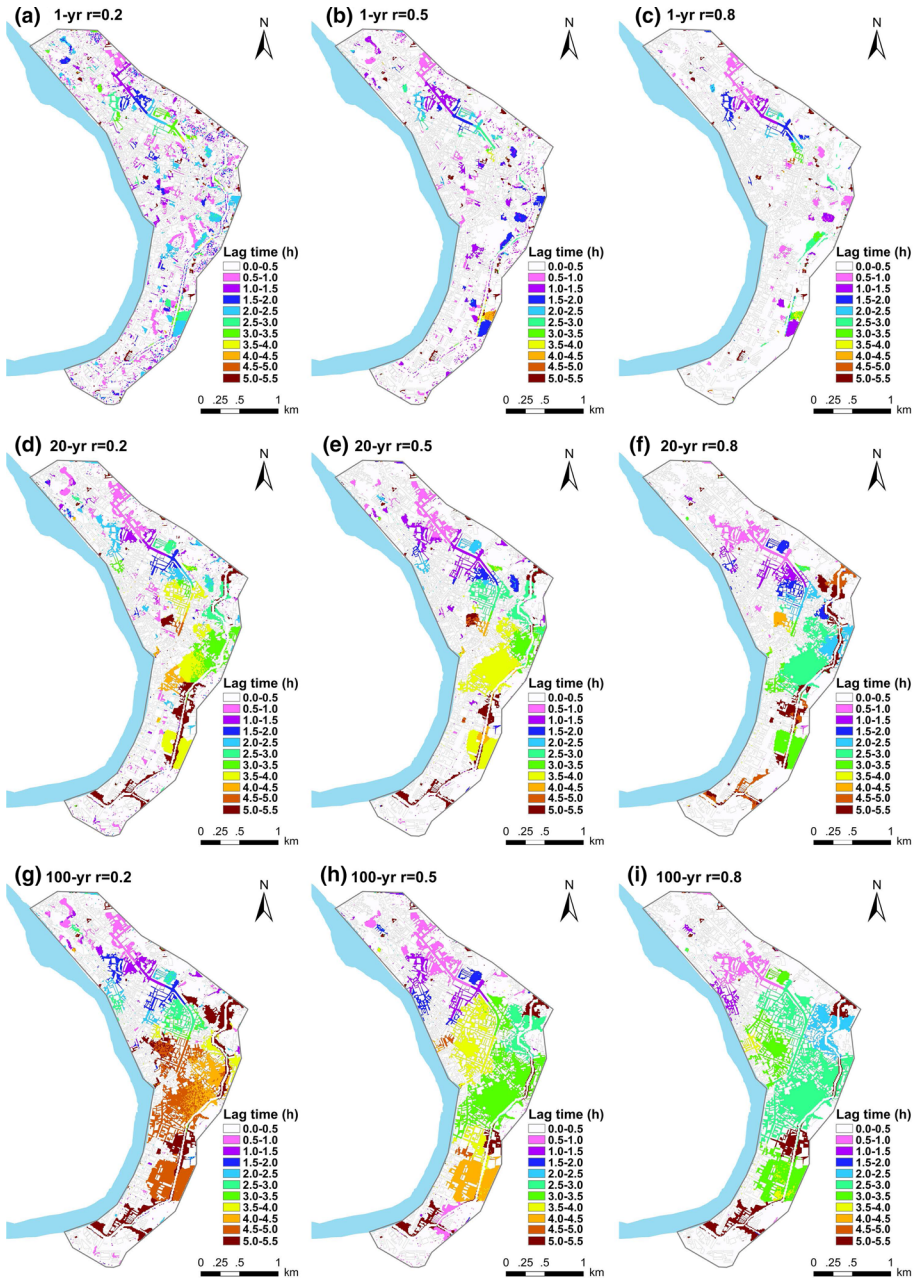


Fig. 11 Spatial distributions of the inundation lag time under different designed rainstorm events for the scenario group (only return periods of 1, 20, and 100 years are presented)

was found when it was encountered by both FF and UW. This can be explained by the fact that the FF dominated the TIV when the return period was larger than 10 years (Fig. 8). As the local rainfall increased the filled ratio of the infiltration and the drainage

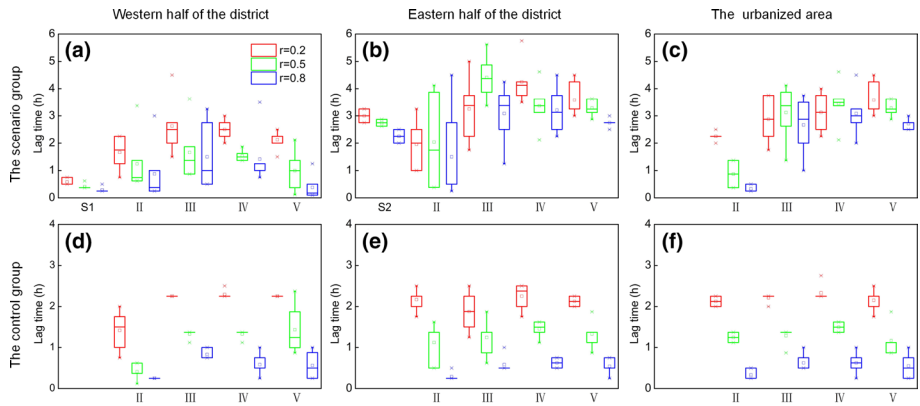


Fig. 12 S1, S2, and inundation hydrograph lag times under three rainstorm patterns for different districts and scenarios (each box plot consists of simulation results for six return periods)

system, there might be minimal volume loss with the FF propagation. The FF almost dominated the TIA within the entire urbanized area thus significantly increasing the surface inundations’ spatial connection, resulting in an excellent relationship that exists between the different low-lying positions under the 18 designed rainstorm events.

$$MID_{FP} = \alpha * EXP(\theta * MID_{RP}) \tag{7}$$

where the intercept α and the exponent θ are the fitting parameters, MID_{RP} is the MID of the reference point, and MID_{FP} is the MID of the other flood-prone points.

Analysis of the R^2 in the scenario group states that the variations of the MID of one specific reference point can explain the variations of the other 30 points. The reference point that we selected is located near the Meixi River and was characterized by short lag times and extremely high inundation depths (Fig. 4). The results show that the MID_{RP} versus MID_{FP} of the other 30 points under the 18 designed rainstorm events follows similar trends. An exponential curve represented in Eq. (7) has been well fitted to this data, with the R^2 ranging from 0.81 to 0.97 (Fig. 13). Each exponential curve for the corresponding point has two parameters intercept α and exponent θ (Eq. (7)). An effort has been made to correlate the α with the θ of the 30 points, which displays a significant negative correlation between the α and the corresponding θ (Fig. 13). The intercept α of each point shows significant spatial variability reflecting the differences in its elevation and location during flooding. The points that are close to the origin of the FF from the S1 sub-basin, the floodplain near the Meixi River channel, and the low-lying areas in the urban center have a larger α and a smaller θ (See the flood-prone points in Fig. 4, the point with a larger size corresponds to a higher α value). Additionally, the exponential relationships were validated by the historical event of rainstorm 20,160,915. We calculated the MID of the ten recorded points based on the MID_{RP} and its exponential relationships to the corresponding ten points. Results of the ten locations show that the relative error of the calculated MID is slightly lower than that of the simulation MID (Table 4). Thus, implying the simple mathematical relationships between the surface inundation locations and can also be used in other actual extreme events with different rainfall intensities and durations.

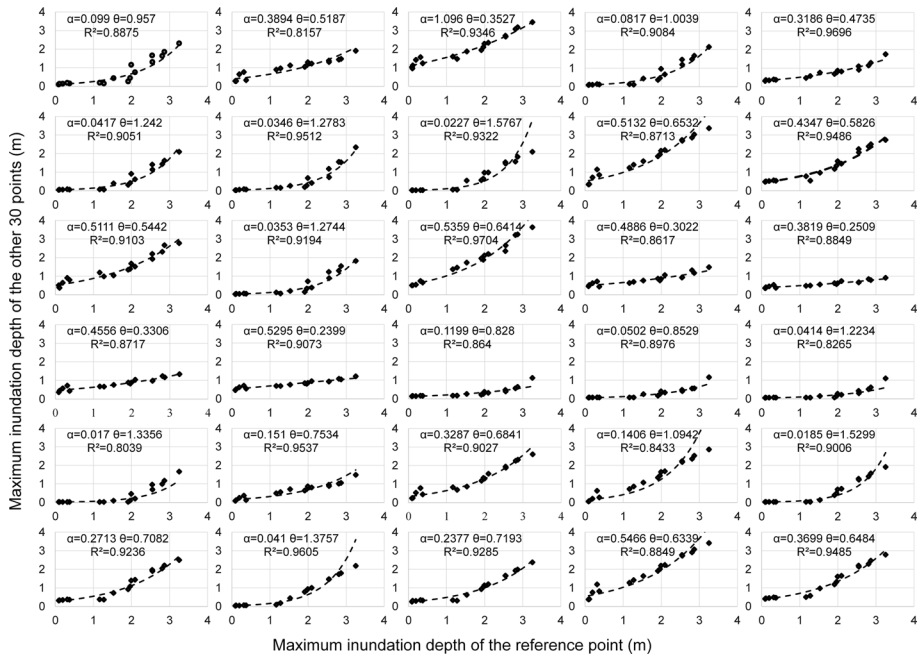


Fig. 13 The exponential relationship of the maximum inundation depth between the reference point and 30 other flood-prone points within the urbanized area

4 Discussion

4.1 Effect of rain patterns and topography on surface inundation

FF hydrographs and surface inundation indicators are primarily concerned with TMA sub-basins and the TUA. Figure 5 and the results of the control group in Fig. 10 revealed that the responses of FF hydrographs and inundation indicators of UW regarding rainstorm characteristics are relatively similar, indicating that the return period (different rainfall intensities and amounts) is the most decisive factor other than the peak coefficients (Cao et al. 2021; Palla et al. 2016; Zhang et al. 2019). The influence of rainstorm patterns is also significant, especially for the FF hydrographs. These impacts are summarized as follows: Higher rain peak coefficients result in greater peak discharges, larger total volumes, and more severe surface inundation. Many studies have revealed the reasons since a higher peak coefficient corresponds to larger soil saturation (Mei et al. 2020) and increased full-filled pipe rates (Chen et al. 2018). Furthermore, our results showed that larger peak coefficients lead to a shorter lag time of both the FF hydrographs and surface inundation. Similar conclusions were also found in previous studies since the peak flood discharge or inundation depth appears faster with a later peak coefficient (Cheng et al. 2020; Yao et al. 2016).

When FF and UW occur simultaneously and superimpose within a short time in the TUA, the response of the surface inundation indicators regarding the rainfall characteristics has some differences compared to the inundation indicators affected only by UW. Previous studies emphasized that the influences and variations caused by rain peak coefficients are negligible in terms of high return period and inundation area with a high-water depth (Mei

et al. 2020; Cheng et al. 2020). In contrast, our results demonstrated that the rain peak coefficients have a greater influence on almost all high return periods and inundation grades. Cao et al. (2021) indicated that the rain patterns have a more significant effect on the discharge hydrographs in high return periods compared to low return periods. Furthermore, the FF aggravates the UW and spatially covers and delays the inundation lag time. Due to the impact of the topography between the western and eastern halves of the districts, the effects of rainstorm patterns on the spatial distributions of inundation depth and lag time are complex with significant discrepancies. Slope and relative elevation are the primary controlling factors of water depth on a smaller scales (Palla et al. 2016; Smart et al. 2016; Zhang et al. 2020). As discussed in Sect. 3.3.4, the spatial distributions of inundation lag time response to rainstorm patterns between the eastern and western halves of the districts can be explained by the contrary slope of the FF propagation pathway. Savage et al. (2016) emphasized that an urban environment where the flood flow pathways overcome topography and get blocked creates greater uncertainty and differences. We know that integrating FF and UW associated with their combined response to rainstorm characteristics has not been well studied or defined. The key findings of this study provide an important reference for flood control and disaster reduction in similar cities located in the alluvial plains of mountainous basins.

4.2 Statistical relationships between flood-prone positions

Researchers and managers may pay more attention to the inundation conditions for some important locations with high FF risk. This study further explores the relationship between spatial inundation depth under 18 differently designed rainfall events. Inundation caused by both FF and UW shows that the MID between the reference point and the 30 other spatially distinct flood-prone points reveals a similar and significant exponential relationship. However, surface inundation without the FF would not be displayed with such good relationships. Chen et al. (2018) and Xing et al. (2021) stated that the inundation volume controls the surface inundation extent and the degree of damage severity. However, with an increase in return periods and peak coefficients, the increment of the flood volume of FF on the sub-basins is significant, and the enhancement and variation of TIV_s are also significant. Once the surface inundation is dominated by FF with several times the volume of UW, the impact to the MID from the underground drainage systems, land cover type, and surface roughness for specific points is minimal. Evidence was introduced by Savage et al. (2016), who demonstrated that the boundary conditions (i.e., input FF hydrographs from mountainous sub-basins in this study) are the most influential factors compared to the DEM data and floodplain roughness in terms of the average maximum water depth and the extent of flooding. Several exponential curve relationships were illustrated between the rainfall characteristics; therefore, the inundation indicates (Haque et al. 2020; Sahoo and Sreeja 2016; Smart et al. 2016; Zhang et al. 2019), compared with previous studies, and the relationships established in this study had an advantage in estimating water inundations for many specific concerning locations. The relationship will be a readymade tool needed to diagnose regional inundations rapidly and efficiently. It will also play an important role in the reduction of early warning times and local property loss.

In this study, although high-resolution input including rainfall design (5 min) and DEM data (1 m) was used for the scenarios, the simulation results also had some uncertainties since the spatial variability of the rainfall data was not considered in the Meixi basin. Our future research will consider the spatial differences of rainfall, the moving speed, and the

direction of the rain mass at the basin scale. Furthermore, we also want to find other small mountainous basins and alluvial plains affected by rapid FFs, in order to verify the universality of the revealed exponential relationships between the spatial inundation depth.

5 Conclusions

This paper uses a coupled hydrologic–hydraulic model to illustrate the flood process response to different rainstorm patterns in a coastal mountainous basin (including five mountainous sub-basins and an urbanized area), within southeastern China. The urbanized area is prone to encounter both external FF and local UW. The FF hydrographs, TIA, inundation areas with varying water depths, inundation lag time, and the relationship of surface inundation MID were investigated based on numerical simulations and scenario analyses under different return periods and rain patterns. The following conclusions were drawn:

- (1) The effect of rain peak coefficients on FF hydrographs and UW inundation indicators is similar for a given return period. The larger the rain peak coefficient is, the greater the peak discharge and total volume produced by the FF hydrographs for all mountainous sub-basins; thus, the more severe the surface inundation that occurs because of UW. The lag time of both the FF hydrographs and the UW inundation decreases with increasing rain peak coefficient. This highlights the prerequisite of considering rain peak coefficients during flood risk mapping and control strategies.
- (2) FF dominates surface inundations for the urbanized area, resulting in the enhanced impact of rain patterns on surface inundation, which are reflected within high return periods and inundation areas with high-water depth. This indicates that FFs have considerably amplified the effects of the rain patterns on surface inundation.
- (3) When the FF and UW are encountered and are superimposed within a short time, the spatial distribution of the inundation depth and lag time showed significant district differences. Our results demonstrated that the increase in inundation risks and the distinctive effects between inundation lag time and rain peak coefficient were affected by the district topography of the FF propagation pathway.
- (4) The dominance of TIV by external FF significantly increases the surface inundation spatial connection of different locations compared with that for UW via local rainfall. A good exponential relationship of MID between the reference point and the other 30 flooding vulnerable points is illustrated even within the different rainstorm intensities and patterns. This finding is a useful tool needed to diagnose regional inundation rapidly and efficiently.

This case study provides a broader understanding of the effects of rainstorm characteristics on inundation indicators by integrating FF and UW in a mountainous basin. The key findings of this study serve as a readymade decision-making tool and thus can aid decision-makers in managing urban flood problems and also presents a more in-depth understanding and technical support for similar mountainous cities that also face the problems of FF and UW.

Acknowledgements This study was jointly supported by the National Natural Science Foundation of China (Grant Nos. 51779007, 41671018). The authors thank AiMi Academic Services (www.aimieditor.com) for the English language editing and review services. We are especially grateful to the two anonymous reviewers for their valuable suggestions, which have improved the quality of the manuscript.

Author contributions Y.J. contributed to conceptualization, methodology, software; J.W. was involved in investigation, resources, data curation, analysis, writing; J.Y. contributed to supervision, project administration, funding acquisition. All authors have read and agreed to the published version of the manuscript.

Data availability The data that support the findings of this study are available from the corresponding author upon reasonable request.

Declarations

Conflicts of interest The authors declare no conflicts of interest.

References

- Bajabaa S, Masoud M, Al-Amr N (2014) Flash flood hazard mapping based on quantitative hydrology, geomorphology and GIS techniques (case study of Wadi AI Lith, Saudi Arabia). *Arab J Geosci* 7(6):2469–2481
- Bayazit Y, Koc C, Bakis R (2021) Urbanization impacts on flash urban floods in Bodrum Province. *Turkey Hydrol Sci J* 66(1):118–133
- Brinkerhoff CB, Gleason CJ, Ostendorf DW (2019) Reconciling at-a-station and at-many-stations hydraulic geometry through river-wide geomorphology. *Geophys Res Lett* 46(16):1–11
- Bruwier M, Mustafa A, Aliaga D, Archambeau P, Erpicuma S, Nishida G, Zhang X, Piroton M, Teller J, Dewals B (2018) Influence of urban pattern on inundation flow in floodplains of lowland rivers. *Sci Total Environ* 622–623:446–458
- Cao X, Qi Y, Ni G (2021) Significant impacts of rainfall redistribution through the roof of buildings on urban hydrology. *J Hydrometeorol* 22(4):1007–1023
- Chen W, Huang G, Han Z, Wang W (2018) Urban inundation response to rainstorm patterns with a coupled hydrodynamic model: A case study in Haidian Island, China. *J Hydrol* 564:1022–1035
- Cheng T, Xu Z, Yang H, Hong S, Leitao JP (2020) Analysis of effect of rainfall patterns on urban flood process by coupled hydrological and hydrodynamic modeling. *J Hydrol Eng* 25(1):04019061
- Chi CC, Mantilla R (2015) Development and analysis of GIS tools for the automatic implementation of 1D hydraulic models coupled with distributed hydrological models. *J Hydrol Eng* 20(12):300–304
- Chouaib W, Alila Y, Caldwell PV (2018) Parameter transferability within homogeneous regions and comparisons with predictions from a priori parameters in the eastern United States. *J Hydrol* 560:24–38
- Dimitriadis P, Tegos A, Oikonomou A, Pagana V, Koukouvinos A, Mamassis N, Koutsyiannis D, Efstratiadis A (2016) Comparative evaluation of 1D and quasi-2D hydraulic models based on benchmark and real-world applications for uncertainty assessment in flood mapping. *J Hydrol* 534:478–492
- Ebrahimian A, Gulliver JS, Wilson BN (2018) Estimating effective impervious area in urban watersheds using land cover, soil character and asymptotic curve number. *Hydrol Sci J* 63(4):513–526
- Gallegos HA, Schubert JE, Sanders BF (2009) Two-dimensional, high-resolution modeling of urban dam-break flooding: A case study of Baldwin Hills. *California Adv Water Resour* 32(8):1323–1335
- Gayer G, Leschka S, Nöhren I, Larsen O, Günther H (2010) Tsunami inundation modelling based on detailed roughness maps of densely populated areas. *Nat Hazards Earth Syst Sci* 10(8):1679–1687
- Grimaldi S, Petroselli A, Arcangeletti E, Nardi F (2013) Flood mapping in ungauged basins using fully continuous hydrologic-hydraulic modeling. *J Hydrol* 487(2):39–47
- Haque MM, Seidou O, Mohammadian A, Djibo AG (2020) Development of a time-varying MODIS/ 2D hydrodynamic model relationship between water levels and flooded areas in the Inner Niger Delta, Mali. *West Africa. J Hydrol* 30:100703
- Hu X, Song L (2018) Hydrodynamic modeling of flash flood in mountain watersheds based on high-performance GPU computing. *Nat Hazards* 91(4):567–586
- Jiang C, Zhou Q, Yu W, Yang C, Lin B (2021) A dynamic bidirectional coupled surface flow model for flood inundation simulation. *Nat Hazards Earth Syst Sci* 21(2):497–515
- Keifer CJ, Chu HH (1957) Synthetic storm pattern for drainage design. *J Hydraul Div* 83(4):1–25
- Kim S, Shen H, Noh S, Seo DJ, Philips B (2021) High-resolution modeling and prediction of urban floods using WRF-Hydro and data assimilation. *J Hydrol* 598:1–14

- Krebs G, Kokkonen T, Valtanen M, Setälä H, Koivusalo H (2014) Spatial resolution considerations for urban hydrological modelling. *J Hydrol* 512(9):482–497
- Leandro J, Schumann A, Pfister A (2016) A step towards considering the spatial heterogeneity of urban key features in urban hydrology flood modelling. *J Hydrol* 535:356–365
- Ma M, Wang H, Jia P, Liu R, Miao L (2018) Investigation of inducements and defenses of flash floods and urban waterlogging in Fuzhou, China, from 1950 to 2010. *Nat Hazards* 91(3):803–818
- Mei C, Liu JH, Wang H, Li ZJ, Yang ZY, Shao WW, Ding XY, Weng BS, Yu YD, Yan DY (2020) Urban flood inundation and damage assessment based on numerical simulations of design rainstorms with different characteristics. *Sci China Technol Sc* 63:2292–2304
- Montanari M, Hostache R, Matgen P, Schumann G, Pfister L, Hoffmann L (2009) Calibration and sequential updating of a coupled hydrologic-hydraulic model using remote sensing-derived water stages. *Hydrol Earth Syst Sci* 13(3):367–380
- Müller H, Haberlandt U (2018) Temporal rainfall disaggregation using a multiplicative cascade model for spatial application in urban hydrology. *J Hydrol* 556:847–864
- O'Brien JS, Julien PY, Fullerton WT (1993) Two-dimensional water flood and mudflow simulation. *J Hydraul Eng* 119(2):244–261
- Palla A, Colli M, Candela A, Aronica G, Lanza L (2016) Pluvial flooding in urban areas: the role of surface drainage efficiency. *J Flood Risk Manag* 11:663–676
- Peng SH, Lu SC (2013) FLO-2D simulation of mudflow caused by large landslide due to extremely heavy rainfall in southeastern Taiwan during Typhoon Morakot. *J Mt Sci* 10(2):207–218
- Sahoo SN, Sreeja P (2016) Relationship between peak rainfall intensity (PRI) and maximum flood depth (MFD) in an urban catchment of Northeast India. *Nat Hazards* 83(3):1–18
- Saksena S, Merwade V (2015) Incorporating the effect of DEM resolution and accuracy for improved flood inundation mapping. *J Hydrol* 530:180–194
- Salvadore E, Bronders J, Batelaan O (2015) Hydrological modelling of urbanized catchments: A review and future directions. *J Hydrol* 529:62–81
- Savage J, Pianosi F, Bates P, Freer J, Wagener T (2016) Quantifying the importance of spatial resolution and other factors through global sensitivity analysis of a flood inundation model. *Water Resour Res* 52(11):9146–9163
- Shang H, Lin B, Xu L (2019) Visualization of precipitation frequency atlas and rainstorm high-risk regionalization atlas. *China Water Wastew* 35(5):131–138 ((in Chinese))
- Shen J, Tan F (2020) Effects of DEM resolution and resampling technique on building treatment for urban inundation modeling: a case study for the 2016 flooding of the HUST campus in Wuhan. *Nat Hazards* 104:927–957
- Smart GM, Crowley K, Lane EM (2016) Estimating Tsunami Run-up. *Nat Hazards* 80(3):1933–1947
- Smith BK, Smith JA, Baeck ML, Villarini G, Wright DB (2013) Spectrum of storm event hydrologic response in urban watersheds. *Water Resour Res* 49(5):2649–2663
- Sun W, Wang J, Li Z, Yao X, Yu J (2014) Influences of climate change on water resources availability in Jinjiang Basin, China. *Sci World J* 282:908349
- Takeuchi K, Hapuarachchi P, Zhou M, Ishidaira H, Magome J (2010) A BTOP model to extend TOP-MODEL for distributed hydrological simulation of large basins. *Hydrol Process* 22(17):3236–3251
- Veldhuis MT, Zhou Z, Yang L, Liu S, Smith J (2018) The role of storm scale, position and movement in controlling urban flood response. *Hydrol Earth Syst Sci* 22:417–436
- Xing Y, Shao D, Ma X, Zhang S, Jiang G (2021) Investigation of the importance of different factors of flood inundation modeling applied in urbanized area with variance-based global sensitivity analysis. *Sci Total Environ* 772(10):145327
- Yang GX, Bowling LC, Cherkauer KA, Pijanowski BC (2011) The impact of urban development on hydrologic regime from catchment to basin scales. *Landsc Urban Plan* 103(2):237–247
- Yang L, Smith JA, Baeck ML, Zhang Y (2016) Flash flooding in small urban watersheds: Storm event hydrologic response. *Water Resour Res* 52(6):4571–4589
- Yao L, Wei W, Chen L (2016) How does imperviousness impact the urban rainfall-runoff process under various storm cases? *Ecol Indic* 60:893–905
- Yin J, Yu D, Yin Z, Liu M, He Q (2016) Evaluating the impact and risk of pluvial flash flood on intra-urban road network: A case study in the city center of Shanghai, China. *J Hydrol* 537:138–145
- Zhang P, Ma J, Shu H, Han T, Zhang Y (2015) Simulating debris flow deposition using a two-dimensional finite model and soil conservation service-curve number approach for Hanlin gully of southern Gansu (China). *Environ Earth Sci* 73:6417–6426
- Zhang Q, Yang Q, Zhang S (2019) Drainage capacity of rainwater pipe network in mountainous urban areas based on SWMM: a case study In Chongqing. *China Fresenius Environ Bull* 28(7):5270–5280

- Zhang QF, Wu ZF, Zhang H, Fontana GD, Tarolli P (2020) Identifying dominant factors of waterlogging events in metropolitan coastal cities: The case study of Guangzhou, China. *J Environ Manage* 271:110951
- Zhao Y, Xia J, Xu Z, Zou L, Qiao Y, Li P (2021) Impact of urban expansion on rain island effect in Jinan City. *North China Remote Sens* 13(15):2989–2989
- Zhou Q, Leng G, Su J, Ren Y (2019) Comparison of urbanization and climate change impacts on urban flood volumes: Importance of urban planning and drainage adaptation. *Sci Total Environ* 658:24–33

Publisher's Note Springer Nature remains neutral with regard to jurisdictional claims in published maps and institutional affiliations.